University of Tehran

Earth Observation and Geomatics Engineering

Online ISSN: 2588-4360

Homepage: https://eoge.ut.ac.ir/

Flood Detection Using Earth Observation Data and a Multi-Stage Fusion via Google Earth Engine: A Case Study of Konarak County, Iran

Behnam Ebadati [1✉], **Mohammad Alikhani**[2], and **Reza Attarzadeh**[3]

1. Corresponding author, Department of Geomatics Engineering, ST.C., Islamic Azad University, Tehran, Iran. E-mail: st_b_ebadati@azad.ac.ir
2. Faculty of Geodesy and Geomatics Engineering, K. N. Toosi University of Technology, Tehran, Iran. E-mail: m.alikhani1@email.kntu.ac.ir
3. Department of Geomatics Engineering, ST.C., Islamic Azad University, Tehran, Iran. E-mail: reza.attarzadeh@iau.ac.ir

Article Info

Article type:
Research Article

Article history:
Received 2026-02-13
Received in revised form 2026-06-01
Accepted 2026-06-01
Available online 2026-07-24

Keywords:
Flood Detection,
Machine Learning,
Decision-Level Fusion,
Multispectral,
SAR,

ABSTRACT

Floods rank among the most destructive natural disasters worldwide, with their frequency and severity escalating due to climate change, rapid urbanization, and land-use changes. Accurate and timely flood detection is critical for effective disaster response and mitigation, especially in vulnerable arid and semi-arid regions frequently affected by flash floods. This study develops a multi-stage fusion framework for flood mapping by integrating Sentinel-1 SAR and Sentinel-2 multispectral data within the Google Earth Engine (GEE) cloud platform. The proposed approach was applied to the extreme flash flood event that struck Konarak County, southeastern Iran, in early January 2022. In the first stage, five supervised machine learning classifiers, including Random Forest (RF), Gradient Boosting Decision Tree (GBDT), Classification and Regression Tree (CART), Support Vector Machine (SVM), and K-Nearest Neighbors (KNN), were independently trained using the fused SAR and optical dataset. In the next stage, Initial flood maps generated by the classifiers were fused at the decision level using the majority voting approach to produce the final flood map. The results show that the decision-level fusion achieved superior performance in terms of statistical metrics. It yielded an overall accuracy of 97.50%, F1-score of 97.42%, and a Kappa coefficient of 0.939, outperforming all individual classifiers considered in this study. In contrast, the RF classifier, which demonstrated the best performance among the classifiers, achieved an overall accuracy of 96.67%, an F1-score of 96.61%, and a Kappa coefficient of 0.933. The proposed method jointly exploits SAR and optical features and combines multiple classifier outputs to improve the accuracy and reliability of flood detection.

Cite this article: Ebadati, B., Alikhani, M., & Attarzadeh, R. (2026). Flood Detection Using Earth Observation Data and a Multi-Stage Fusion via Google Earth Engine: A Case Study of Konarak County, Iran. *Earth Observation and Geomatics Engineering*, Volume 10, Issue 1, Pages 70-82. http//doi.org/10.22059/eoge.2026.411063.1217

Publisher: University of Tehran.
DOI: http//doi.org/10.22059/eoge.2026.411063.1217

1. Introduction

Floods are among the most devastating natural disasters, and their frequency and severity have significantly increased due to climate change. This natural disaster has caused extensive damage by destroying or severely impairing infrastructure, disrupting agricultural and economic activities, and leading to loss of life. The scale of these damages continues to rise as floods repeatedly occur in various regions around the (Brémond et al., 2013; Colacicco et al., 2024; Dottori et al., 2018; Willner et al., 2018). The rapid expansion of urbanization and land-use changes are among the most significant factors contributing to flood occurrence. Nevertheless, intense or prolonged rainfall is considered the primary triggering factor in the emergence of severe flooding events (Yu et al., 2022).

Although floods can occur in all parts of the globe, their intensity varies depending on the geographical features and topography of each region (Liu & Huang, 2020). Moreover, the extent of flood-induced damage is directly related to the level of infrastructure development and the effectiveness of disaster management within communities. In other words, developed countries generally suffer less damage compared to less developed nations. While the impact in developed countries is often limited to economic losses, less developed countries not only face widespread economic damage but also endure higher casualties and more severe social consequences (Stucchi et al., 2021; Tariq et al., 2020). Therefore, it is foreseeable that the location of a less developed country in a region that is prone to severe flooding due to its geographical conditions can lead to catastrophic events. Iran is one such country.

Access to up-to-date and accurate flood information can greatly enhance disaster management efforts. Remote sensing plays a crucial role in this regard (Amitrano et al., 2018). Today, a variety of satellite sensors with diverse capabilities continuously orbit the Earth, observing its surface (Amitrano et al., 2024). As a result, obtaining real-time and cost-effective information for flood monitoring and mapping affected areas has become highly feasible (Giustarini et al., 2016; Martinis et al., 2015). In particular, data obtained from Synthetic Aperture Radar (SAR) sensors allows users to monitor flood conditions around the clock, even in adverse weather conditions (Chini et al., 2021). Since SAR systems actively emit microwave signals, they operate independently of sunlight and are capable of penetrating cloud cover, rainfall, and atmospheric disturbances, which are commonly associated with flood events (Lang et al., 2024; Uddin et al., 2019; Voormansik et al., 2014). The complementary nature of SAR and optical sensors makes their combined use especially advantageous for flood mapping and monitoring. While SAR data are well-suited for flood detection during active events due to their all-weather imaging capability, optical imagery contributes valuable contextual and spectral information when atmospheric conditions permit (Qin et al., 2025; Tavus et al., 2020). Moreover, the strong contrast between smooth water surfaces and surrounding terrain in SAR imagery, caused by specular scattering of microwave signals, facilitates reliable flood delineation (Landuyt et al., 2019; Manavalan, 2016; Shen et al., 2019).

Recent advances in machine learning have significantly enhanced the ability to analyze large-scale remote sensing data by enabling automated feature extraction, pattern recognition, and robust classification of complex land surface phenomena (Kazanskiy et al., 2025; Zaka & Samat, 2024). Machine learning algorithms are particularly effective in flood mapping applications, where they can integrate multi-source satellite data and learn discriminative representations of inundated and non-inundated areas with high accuracy. However, the increasing volume, spatial coverage, and temporal frequency of satellite observations pose substantial computational and storage challenges (Manyaka et al., 2026; Wagner et al., 2026). Cloud-based processing platforms address these limitations by providing scalable computing resources and direct access to extensive geospatial data archives (Sellami & Rhinane, 2024). Among these platforms, Google Earth Engine (GEE) has emerged as a powerful cloud-based geospatial analysis environment, offering a vast catalog of preprocessed satellite imagery, including both SAR and optical data, along with parallel computing capabilities. By combining machine learning techniques with cloud-based processing in GEE, it becomes possible to efficiently perform large-scale flood monitoring and mapping with reduced computational cost and improved timeliness (Hajji et al., 2025; Peng et al., 2025; Tian et al., 2026).

Recent studies have advanced flood mapping by fusing Sentinel-1 SAR and Sentinel-2 optical imagery using traditional machine learning algorithms such as Random Forest and Support Vector Machine within GEE. This approach enables scalable, efficient flood detection by leveraging complementary all-weather SAR capabilities and spectral information. Razzano et al. (2023) integrated Sentinel-1 backscatter features with Sentinel-2 spectral bands and indices in GEE using supervised machine learning algorithms for Earth surface classification, with water bodies included as one of the classes. Their results demonstrate that fusing radar and optical data improves overall classification accuracy by exploiting complementary information from all-weather SAR and multispectral optical sources (Razzano et al., 2023). Ganjirad and Delavar (2023) implemented Random Forest and Support Vector Machine models in GEE for flood risk mapping, fusing Sentinel-1 SAR-derived flood extent with Sentinel-2 spectral indices alongside topographic factors to evaluate susceptibility in Louisiana, USA (Ganjirad & Delavar, 2023). Yassine et al. (2024) conducted a comparative study of flood mapping methodologies within Google Earth Engine using Sentinel-2 and Landsat imagery alongside Sentinel-1 SAR data for the Tetouan flood event, incorporating machine learning refinements such as Random Forest to improve accuracy over basic thresholding (Yassine et al., 2024). Farhadi et al. (2025) presented an automatic time-series flood mapping framework using Sentinel-1 and Sentinel-2 imagery on GEE with machine learning classifiers for change detection, supporting near-real-time monitoring by integrating complementary SAR and optical features (Farhadi et al., 2025). These works demonstrate GEE's effectiveness in facilitating machine learning-driven fusion of Sentinel-1 and Sentinel-2 for practical flood applications, emphasizing non-deep learning methods for computational efficiency and interpretability.

In this study, a multi-stage fusion framework is proposed within the GEE environment to simultaneously exploit the capabilities of SAR and optical remote sensing data along with machine learning algorithms. This study is fully GEE-based, leveraging its cloud-computing capabilities for data preprocessing, model training, and fusion. The proposed framework consists of two main stages, as depicted in Figure 1. In the first stage, SAR and optical data are fused to generate a unified set of spatial and backscatter/spectral features for training the classifiers. Based on the fused data, five supervised machine learning algorithms available in GEE are independently trained, and initial flood detection maps are generated. In the second stage, the outputs of individual classifiers are combined at the decision level to reduce uncertainty. This produces a final flood detection map, enabling the combined use of multiple machine learning algorithms. For comparison, two deep learning models, U-Net++ and SegNet, were implemented outside the GEE framework using Keras. These models were trained on the same dataset to benchmark the performance of the proposed GEE-based method against recent deep learning approaches.

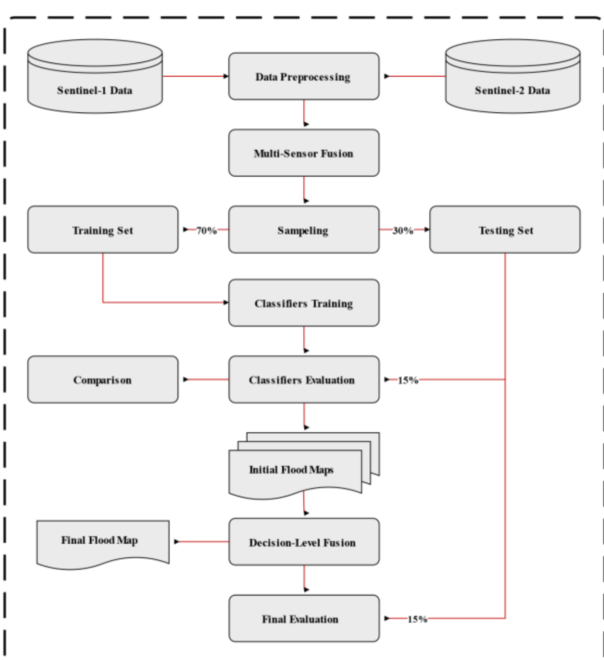

Figure 1. Methodology flowchart

2. Methodology

2.1. Study Area

Konarak County, located in Sistan and Baluchestan Province in southeastern Iran, has been selected as the study area for this research. The region experiences a warm and relatively dry climate for most of the year. However, due to its location along the coast of the Oman Sea, it is frequently exposed to sea storms and intense rainfall systems (Zainudini & Sardarzaei, 2023). In early January 2022, Konarak and its neighboring areas experienced extreme rainfall, with 100 millimeters recorded in just 20 minutes. This event caused widespread inundation of urban areas and severe flooding in agricultural lands and rural settlements. Figure 2 shows the geographical location of the study area. The post-event conditions following the January 2022 rainfall are shown based on a Sentinel-2 false color composite, where red pixels indicate flooded areas and zones of high surface moisture.

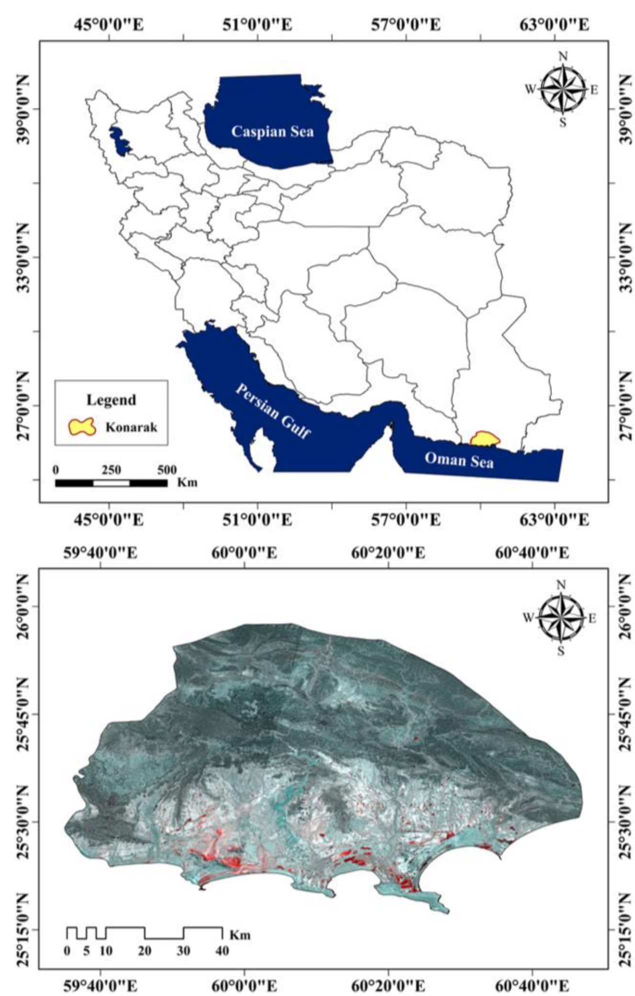

Figure 2. Geographic location of Konarak County and the flood-affected area

2.2. Data

The data used in this study consist of SAR and multispectral imagery acquired from the Sentinel-1 and Sentinel-2 missions. The datasets correspond to the studied flood event and were obtained from the GEE data catalog for the period spanning 1 to 10 January 2022.

2.2.1. Sentinel-1

The Sentinel-1 mission consists of two separate satellites, named Sentinel-1A and Sentinel-1 B. Both satellites are equipped with Synthetic Aperture Radar (SAR) sensors operating in the C-band. These sensors are capable of providing images with a swath width of 250 kilometers and a spatial resolution ranging from 10 to 20 meters in Interferometric Wide Swath (IW) mode. The simultaneous operation of these two satellites provided a 6-day revisit cycle until Sentinel-1B was decommissioned in 2021 due to a technical malfunction. Currently, Sentinel-1 mission data remains the only SAR data with completely open access (Torres et al., 2012).

2.2.2. Sentinel-2

The Sentinel-2 mission consists of two twin satellites, Sentinel-2A and Sentinel-2B, carrying a multispectral optical sensor known as the Multispectral Instrument (MSI). The MSI sensor acquires imagery in 13 spectral bands spanning the visible, near-infrared, and shortwave infrared regions of the electromagnetic spectrum, with spatial resolutions of 10, 20, and 60 meters depending on the spectral band. The combined operation of Sentinel-2A and Sentinel-2B ensures a global revisit time of 5 days at the equator. Sentinel-2 data are freely and openly accessible, making them widely used for land surface monitoring, environmental analysis, and disaster assessment applications (Drusch et al., 2012).

2.3. Data Preprocessing

The Sentinel-1 and Sentinel-2 data were preprocessed to ensure compatibility and quality for subsequent analysis. For Sentinel-1, essential preprocessing steps, including radiometric and geometric corrections as well as conversion of pixel backscatter values from linear to logarithmic scale (dB), were already applied by default in the GEE. To reduce speckle noise, a median filter with a circular kernel of 30 meters radius was applied to both VV and VH polarizations. For Sentinel-2, preprocessing included cloud masking to remove cloud-affected pixels and scaling reflectance values by a factor of 0.0001. Furthermore, the Aerosol, Water Vapor, and Cirrus bands were removed from the feature set. All Sentinel-1 and Sentinel-2 bands were then resampled to a common spatial resolution of 20 meters using bilinear interpolation. Next, a composite image for each sensor was generated by averaging all available images acquired over the study area from January 1 to 10, 2022, coinciding with the flood peak. Finally, the composites were clipped to the Konarak county boundary.

2.4. Multi-Sensor Fusion

Upon completion of preprocessing, the Sentinel-1 and Sentinel-2 data were fused to leverage the complementary information provided by each sensor. For this purpose, the selected bands from each sensor, as listed in Table 1, were reprojected to a common spatial reference. Subsequently, these bands were stacked to form an integrated dataset containing all aligned spatial and backscatter/spectral features. This simple multi-sensor fusion approach enables machine learning classifiers to simultaneously exploit both SAR and optical information, leading to improved classification accuracy. Unlike more complex fusion techniques such as Principal Component Analysis (PCA) or wavelet transforms, band stacking is simpler and more reproducible. These advanced fusion methods often require intensive computations and are not straightforward to implement in GEE.

Table 1. Sentinel-1 and Sentinel-2 bands used for fusion.

ID	Sensor	Band/Polarization	Resolution (m)
1	Sentinel-1	VV	Resampled to 20
2	Sentinel-1	VH	Resampled to 20
3	Sentinel-2	Band 2 - Blue	Resampled to 20
4	Sentinel-2	Band 3 - Green	Resampled to 20
5	Sentinel-2	Band 4 - Red	Resampled to 20
6	Sentinel-2	Band 5 - Red Edge 1	20
7	Sentinel-2	Band 6 - Red Edge 2	20
8	Sentinel-2	Band 7 - Red Edge 3	20
9	Sentinel-2	Band 8 – NIR	Resampled to 20
10	Sentinel-2	Band 8A - Red Edge 4	20
11	Sentinel-2	Band 11 - SWIR 1	20
12	Sentinel-2	Band 12 - SWIR 2	20

2.5. Sampling

For training the classifiers and assessing the accuracy of the results, a total of 800 sample points were collected from the study area, equally distributed between the flood and non-flood classes to ensure class balance. The spectral and backscattering features extracted from the fused dataset at these sample points were used as input for training the classifiers. The samples were divided into three independent sets with no overlap. Of the total samples, 70% were allocated for training the classifiers. The remaining 30% were split into two equal parts, with 15% utilized to assess the performance of the classifiers and 15% for decision-level fusion evaluation.

2.6. Applied Machine Learning Classifiers

GEE provides the capability to implement common machine learning algorithms through ready-made scripts, making it easier to apply these algorithms to remote sensing data. In addition, the GEE API allows for the customization of hyperparameters, enabling fine-tuning of the algorithms according to specific requirements. In this study, five widely used classifiers were employed, and Table 2 presents their key hyperparameters.

2.6.1. Random Forest

Random Forest (RF) is an ensemble machine learning algorithm based on a collection of decision trees constructed using random subsets of training samples and input features. Each tree is trained independently, and the final classification result is obtained through majority voting among all trees. This ensemble strategy reduces overfitting and improves model robustness against noise. Due to its ability to model complex nonlinear relationships and handle high-dimensional data, RF has been widely applied in various machine learning classification tasks (Hitouri et al., 2024).

2.6.2. Gradient Boosting Decision Tree

Gradient Boosting Decision Tree (GBDT) is an ensemble learning technique that builds a strong classifier by combining multiple weak decision trees. Unlike Random Forest, which trains trees independently, Gradient Boosting trains trees sequentially, with each tree correcting the errors made by the previous one. The algorithm minimizes a loss function by adjusting the weights of misclassified samples, making it highly effective in improving model performance. GBDT is known for its high predictive accuracy and ability to handle complex datasets with strong non-linear relationships. It is often used in regression and classification tasks where precision is critical (Dudy et al., 2025).

2.6.3. CART

Classification and Regression Tree (CART) is a decision tree-based algorithm that recursively partitions the input data into increasingly homogeneous subsets using impurity-based splitting criteria. CART offers a transparent and interpretable structure, allowing insight into the decision-making process and the relative importance of input features. However, as a single-tree model, it can be sensitive to noise. Despite this limitation, CART remains a useful and interpretable baseline method for comparison with more advanced classification algorithms (Shakya et al., 2021). For this classifier, the hyperparameters were set to their default values in the GEE API, and no custom tuning was applied.

2.6.4. Support Vector Machine

Support Vector Machine (SVM) is a supervised learning algorithm that aims to identify an optimal hyperplane that maximizes the margin between different classes. By employing kernel functions, SVM can effectively handle nonlinear class boundaries by projecting the input data into a higher-dimensional feature space. Owing to its strong generalization capability and effective performance with limited training samples, SVM has been extensively used in image classification (Mohajane et al., 2021).

2.6.5. K-Nearest Neighbours

K-Nearest Neighbors is a simple, non-parametric classification algorithm that assigns class labels based on the majority class among the K closest training samples in the feature space. The performance of KNN strongly depends on the choice of distance metric and the value of K. Although computationally straightforward, KNN can provide competitive results when appropriate feature representations are used and is often employed as a baseline method in supervised classification studies (Rahman et al., 2025; Razavi-Termeh et al., 2024).

Table 2. Key hyperparameters of the classifiers.

Classifier	Hyperparameter	Value
RF	n of Trees	50
GBDT	n of Trees / Learning Rate	50 / 0.01
CART	-	-
SVM	Kernel / C / Gamma	RBF / 0.1 / 0.5
KNN	K	5

2.7. Decision-Level Fusion

In this study, decision-level fusion was applied to combine the initial results obtained by the classifiers. Decision-level fusion is a technique that merges the outputs of multiple classifiers to improve classification accuracy by leveraging the complementary strengths of individual classifiers. Each classifier generates a result for the same data, and these results are then merged to produce a final decision. The goal of decision-level fusion is to reduce uncertainty and enhance classification robustness by integrating diverse classifier predictions (Le Bris et al., 2019). For this purpose, a majority voting approach was used, where the final class for each pixel is determined by the most frequent class among the classifier outputs.

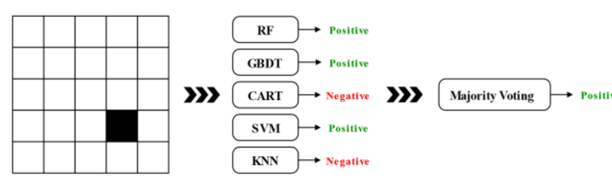

Figure 3. Majority voting fusion scheme

For instance, if one classifier assigns a pixel to the "flood" class, another to "non-flood," and the third to "flood," the majority-voting method will classify that pixel as "flood" by majority rule. Since the number of classifiers in this study is odd, a clear majority is always reached, ensuring a definitive final result without ambiguity, as depicted in Figure 3.

2.8. Accuracy Assessment Procedure

The accuracy of the classifiers was evaluated using 15% of the sample points reserved for this purpose. To assess the performance of classifiers, commonly used metrics, including Overall Accuracy, Precision, Recall, F1-Score, and Kappa Coefficient, were employed, all of which can be calculated within the GEE environment. Furthermore, to evaluate the accuracy of the final results obtained from decision-level fusion, the remaining 15% of the sample points were utilized.

2.8.1 Overall Accuracy

Overall Accuracy evaluates the general performance of a classifier by indicating the proportion of correctly classified samples among all evaluated samples, regardless of class. It provides an overall measure of classification correctness. The Overall Accuracy is defined as:

$$Overall\ Accuracy = \frac{TP + TN}{TP + TN + FN + FP} \tag{1}$$

Where TP, TN, FP, and FN denote true positive, true negative, false positive, and false negative values (Morales-Barquero et al., 2019).

2.8.2 Precision

Precision measures the reliability of positive predictions by indicating the proportion of correctly predicted positive samples among all samples classified as positive (Vongkusolkit et al., 2023). The Precision is defined as:

$$Precision = \frac{TP}{TP + FP} \tag{2}$$

2.8.3 Recall

Recall reflects the ability to correctly identify positive samples by representing the proportion of correctly detected positive samples among all actual positive samples (Popandopulo et al., 2023). The Recall is defined as:

$$Recall = \frac{TP}{TP + FN} \tag{3}$$

2.8.4 F1-Score

The F1-score is a widely used performance metric for evaluating classification results, particularly in applications involving imbalanced classes. It provides a balanced measure of classifier performance by jointly reflecting different types of classification errors (Hinojosa Lee et al., 2024). The F1-score is defined as:

$$F1 - Score = \frac{TP \times 2}{TP + FP + FN \times 2} \tag{4}$$

2.8.5 Kappa Coefficient

The Kappa Coefficient indicates the level of agreement between the classified results and reference data, while accounting for the possibility of random agreement (Cohen, 1960). The Kappa Coefficient is defined as:

$$Kappa\ Coefficient = \frac{P_o + P_e}{1 - P_e} \tag{5}$$

where P_o is the observed accuracy, and P_e is the expected accuracy under random chance.

2.9. Deep Learning Models

To benchmark the employed GEE-based machine learning models with decision-level fusion in this study, two deep learning models were trained using the same dataset over the Konarak region. These models, inspired by U-Net++ and SetNet architectures, were implemented outside the GEE framework, considering hardware limitations. Both models were trained using the same configuration with 50 epochs, a learning rate of 0.001, the Adam optimizer, and categorical cross-entropy as the loss function. Their performance was evaluated using the same evaluation metrics employed in this study. The results obtained from these models are presented solely for comparative purposes and do not contribute to the final findings of this study.

2.9.1. U-Net++

U-Net++ is a nested and densely connected extension of the original U-Net. It refines skip connections through intermediate convolutional layers. This reduces the semantic gap between encoder and decoder representations (Zhou et al., 2018). In the custom architecture used in this study, the encoder has five levels with filter sizes from 8 to 128, and each convolutional block contains two Conv2D layers. These are followed by BatchNormalization and ReLU activation. The nested decoder employs dense skip connections. These concatenate feature maps from multiple preceding levels at each decoder node. The nested decoder employs dense skip connections that concatenate feature maps from multiple preceding levels at each decoder node.

2.9.2. SegNet

SegNet is an encoder-decoder architecture designed for pixel-wise semantic segmentation. It stores max-pooling indices during encoding and uses them for up-sampling during decoding (Badrinarayanan et al., 2017). Similar to U-Net++, the custom architecture in this study has an encoder with five levels, filter sizes from 8 to 128, and two Conv2D layers per block followed by BatchNormalization and ReLU activation. The decoder uses the stored pooling indices from the corresponding encoder level to up-sample feature maps back to the original input resolution.

3. Results

3.1. Machine Learning Classifiers Performance Analysis

The statistical performance metrics of the classifiers are presented in Table 3. The RF achieves the best statistical results, with the highest overall accuracy of 96.67%, precision of 96.72%, recall of 95%, F1-score of 96.61%, and Kappa coefficient of 93.34%, reflecting its excellent balance of classification performance and strong agreement beyond chance. The GBDT ranks second with highly competitive scores of 95.83% accuracy, 95.08% precision, 96.67% recall, 95.86% F1-score, and 91.24% Kappa, demonstrating robust capability in modeling complex patterns and serving as a strong alternative to RF.

Table 3. Statistical metrics values of machine learning classifiers.

Metric/Classifier	RF	GBDT	CART	SVM	KNN
Overall Accuracy	96.67	95.83	83.19	94.17	89.58
Precision	96.72	95.08	84.48	93.44	87.30
Recall	95.00	96.67	81.67	94.91	91.07
F1-Score	96.61	95.86	83.02	94.18	89.39
Kappa Coefficient	93.34	91.24	78.55	89.30	84.71

The CART exhibits the weakest performance among the classifiers, recording 83.19% accuracy, 84.48% precision, 81.67% recall, 83.02% F1-score, and 78.55% Kappa, which underscores the limitations of a single decision tree in capturing intricate data relationships without ensemble techniques. The SVM delivers solid third-place results with 94.17% accuracy, 93.44% precision, 94.91% recall, 94.18% F1-score, and 89.30% Kappa, providing a reliable option when margin-based separation and balanced precision–recall trade-offs are desired. The KNN shows moderate performance at 89.58% accuracy, 87.30% precision, 91.07% recall, 89.39% F1-score, and 84.71% Kappa, making it less competitive than ensemble or kernel-based methods in this context, likely due to sensitivity to feature scaling and dimensionality. In summary, ensemble-based approaches, led by RF and followed closely by GBDT, demonstrate consistent superiority across all metrics.

3.2. Comparison with Deep Learning Models

Table 4 presents the performance evaluation results of the deep learning models U-Net++ and SegNet. Neither model exceeded 80% overall accuracy, with U-Net++ achieving 79.23% and SegNet 74.68%. Their precision values were 78.86% and 73.52%, recall values 74.91% and 71.23%, F1-scores 77.85% and 72.36%, and Kappa coefficients 58.50% and 51.29%, respectively. In contrast, all machine learning classifiers achieved substantially higher accuracies, as shown in Table 3.

Notably, even the relatively weaker classifiers in this study, namely CART with 83.19% and KNN with 89.58%, outperformed U-Net++ and SegNet models across all metrics. This performance gap was even more pronounced when compared to the RF, GBDT, and SVM classifiers. These classifiers outperformed U-Net++ and SegNet by approximately 15-17% and 19-22% in accuracy, respectively, despite being trained on the same shared training samples.

Table 4. Statistical metrics values of deep learning models.

Model	U-Net++	SegNet
Overall Accuracy	79.23	74.68
Precision	78.86	73.52
Recall	74.91	71.23
F1-Score	77.85	72.36
Kappa Coefficient	58.50	51.29

3.3. Decision-Level Fusion Performance Analysis

The decision-level fusion based on the majority voting strategy achieved an overall accuracy of 97.50%, precision of 98.28%, recall of 98.33%, F1-score of 97.42%, and a Kappa coefficient of 93.89. Compared to the individual classifiers, the fused result slightly outperforms the RF, the best-performing classifier, in overall accuracy and recall, while maintaining comparable performance across other metrics. The comparative performance of voting and all classifiers is shown in Figure 4. More precisely, the fusion increases overall accuracy by approximately 0.8% and recall by 3.3%, with modest gains of 0.8% in F1-score and 0.6% in Kappa, indicating reliability of the classification.

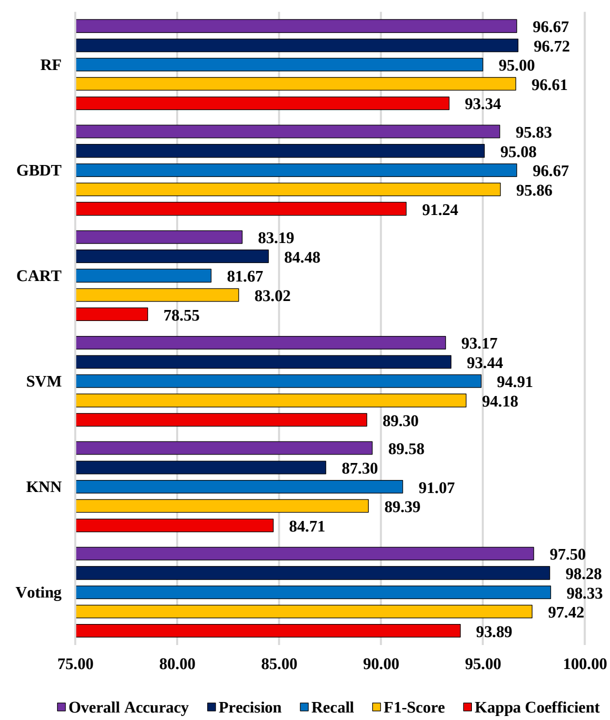

Figure 4. Performance comparison of the voting and classifiers

Table 5. Entropy and uncertainty values by agreement level.

Agreement Level	Vote Count		Entropy	Uncertainty
	Flood	Non-Flood		
Complete	5	0	0.00	None
Complete	0	5	0.00	None
High	4	1	0.72	Low
High	1	4	0.72	Low
Moderate	3	2	0.97	Moderate
Moderate	2	3	0.97	Moderate

Table 5 presents the entropy values and associated uncertainty levels for the decision-level fusion results across three agreement levels, separately for flood and non-flood classes. At the Complete agreement level, all five classifiers

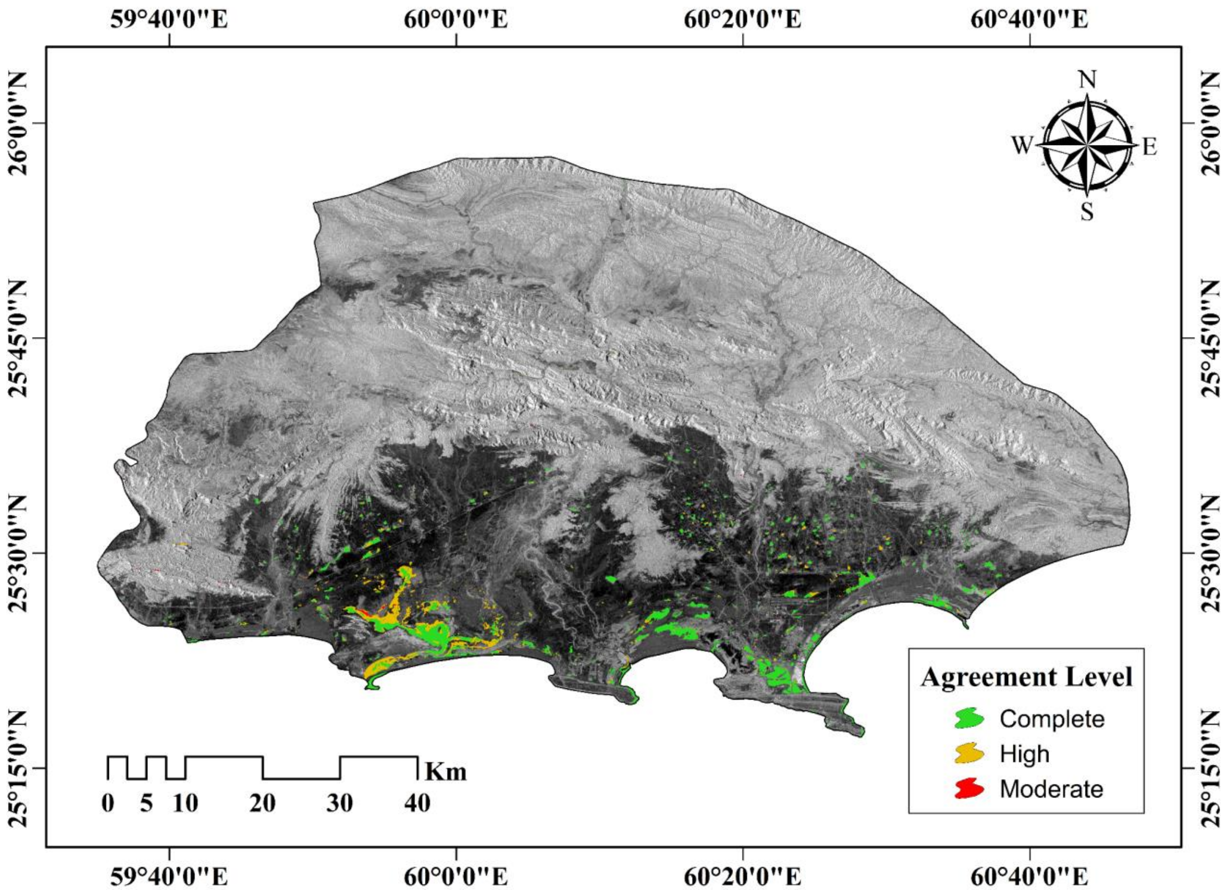

Figure 5. Agreement level map for flooded areas

unanimously agreed on either flood or non-flood class, resulting in an entropy of 0 and no uncertainty.

At the High agreement level, four classifiers voted for the majority class and one voted against it, representing a 4:1 vote distribution. This level corresponds to an entropy of 0.72 and low uncertainty. At the Moderate agreement level, three classifiers voted for the majority class and two voted against it, resulting in a 3:2 split. This level yields the highest entropy value of 0.97 and moderate uncertainty. For a clearer interpretation, the agreement map is shown in Figure 5, where non-flood pixels have been masked to concentrate exclusively on flooded areas. Flood pixels with complete agreement, shown in green, accounted for 202,816 pixels, covering more than 66% of the total 305,709 flood pixels. The high agreement level, colored in yellow, ranked second in frequency with 99,081 pixels, representing 32.41% of the total flood pixels. The moderate agreement level, shown in red, accounted for the remaining 3,812 pixels, or 1.25% of the flood area.

Table 6. Flooded area distribution by agreement level.

Agreement Level	Pixel Count	Area (Km^2)	Area (%)
Complete	202,816	81.13	66.34
High	99,081	39.63	32.41
Moderate	3,812	1.52	1.25
Total	305,709	122.28	100

3.4. Flood Extent Visualization

Figure 6 shows the final flood map of Konarak County in January 2022, derived from the proposed multi-stage fusion framework. Flooded areas, displayed in red polygons, covered approximately 122.28 km^2 of the county. These areas were mainly concentrated in the southern parts of Konarak County, where the greatest impact occurred following the heavy rainfall of January 2022. Specifically, Konarak port city, located at the southernmost edge of the county, experienced widespread flooding along its urban margins. Inset A provides a more detailed representation of the flooded urban and peri-urban areas, alongside Sentinel-1 VV polarization and Sentinel-2 true-color composite of the same area. Additionally, flooding of airport infrastructure and nearby agricultural lands north of Konarak city is notable. Inset B also provides visual details of the flooded rugged terrain, where the interaction of floodwater with irregular topography is clearly observable. SAR backscatter, optical reflectance, and the final flood map show strong visual consistency. This confirms that majority voting fusion effectively separates temporary floodwater from non-flooded surfaces in this semi-arid coastal environment.

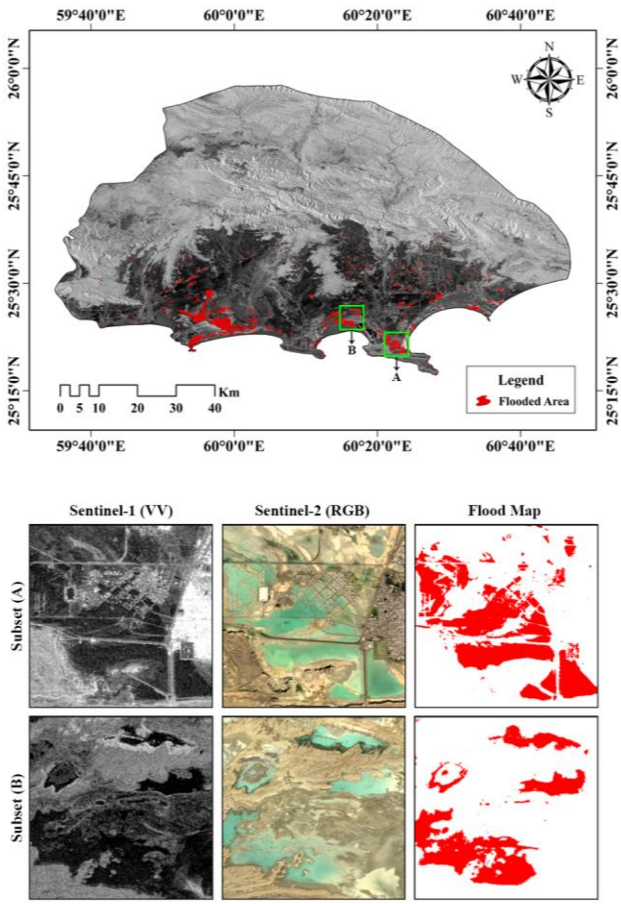

Figure 6. Flood map of Konarak County, January 2022

4. Discussion

The multi-stage fusion framework for flood mapping initially integrates Sentinel-1 SAR and Sentinel-2 multispectral data within GEE. The approach fuses SAR and optical features at the data level. It then applies decision-level fusion using majority voting across five machine learning classifiers to enhance the accuracy and reliability of flash flood detection in arid regions such as Konarak County, Iran. The decision-level fusion achieved an overall accuracy of 97.50%, F1-score of 97.42%, and Kappa coefficient of 0.939. This performance surpasses all individual classifiers.

Among the individual classifiers, RF demonstrated the highest performance, achieving an overall accuracy of 96.67% and a Kappa coefficient of 0.933. GBDT and SVM followed with slightly lower but comparable accuracies, whereas CART showed substantially weaker performance, with an overall accuracy of about 83%. KNN exhibited moderate results, confirming that ensemble- and margin-based methods are generally more effective for flood detection using fused SAR and optical data. Ensemble-based classifiers like RF and GBDT handled complex relationships in fused datasets effectively, outperforming simpler models like CART.

To benchmark the proposed method against deep learning, U-Net++ and SegNet were implemented in Keras using the same training data. Both models achieved overall accuracies below 80%, with U-Net++ at 79.23% and SegNet at 74.68%. The weaker performance of deep learning models stems from the limited number of training samples, which was 560 points, as deep architectures typically require large-scale data. In contrast, machine learning classifiers can achieve acceptable performance even with a limited number of training samples, as demonstrated by all classifiers used in this study. This confirms that traditional machine learning is more data-efficient for flood mapping with scarce reference points.

Despite the strong performance of individual classifiers such as RF, no single classifier is perfect. A higher overall statistical performance of a single classifier does not necessarily guarantee correct classification for every pixel. For instance, a weaker classifier may correctly predict certain target pixels where a stronger classifier fails. Therefore, combining the outputs of multiple classifiers through decision-level fusion can improve the reliability and robustness of the final classification results. The decision-level fusion improved performance over the best individual classifier by increasing overall accuracy by 0.83% and recall by 3.33%, while providing comparable results in other metrics. This improvement arises from the majority voting mechanism that resolves discrepancies among classifier outputs. Beyond overall accuracy improvement, the proposed framework provides insight into classification uncertainty through agreement level analysis. The final flood map was generated by majority voting among five classifiers, producing three agreement levels: Complete for 5:0 votes, High for 4:1 votes, and Moderate for 3:2 votes. Entropy values of 0.00, 0.72, and 0.97 correspond to these levels, representing no, low, and moderate uncertainty, respectively. Analysis of the flooded area revealed that more than 66% of flood pixels showed complete agreement, while only 1.25% exhibited moderate agreement. This uncertainty assessment enhances the interpretability of the final flood map and supports informed decision-making for emergency response.

To contextualize the results, comparisons with three studies that employed multi-level fusion strategies in remote sensing classification are provided. The framework proposed in this study outperforms these approaches in terms of overall accuracy. This improvement can be attributed to the multi-stage fusion strategy, which integrates data-level and decision-level fusion to effectively reduce classification errors across heterogeneous and complex landscapes. Similar trends have been reported in previous studies that explored multi-level fusion strategies in remote sensing applications. Zhong et al. (2017) proposed ODF-ADE as a pure decision-level fusion method for urban land use and land cover classification, achieving an overall accuracy of 93.5% (Zhong et al., 2017). Building on this concept, Zhang et al. (2023) introduced the Feature–Decision Level Collaborative Fusion Network (FDCFNet), which combines feature-level and decision-level fusion for hyperspectral and LiDAR data, reporting overall accuracies of 96.61% on the Houston dataset, 99.11% on the Trento dataset, and 92.90% on the MUUFL Gulfport dataset (Zhang et al., 2023). In addition, Irfan et al. (2025) investigated the fusion of SAR and optical data using a dual-branch convolutional neural network on the SEN12MS dataset and demonstrated that early fusion achieved higher accuracy than decision-level fusion, with overall accuracies of 88.12% and 83.96%, respectively (Irfan et al., 2025).

Overall, the findings of this study demonstrate that multi-stage fusion not only improves statistical performance but also enhances the robustness of classification. The combination of complementary backscatter and spectral features from SAR and optical with classifier diversity provides a more reliable representation of the flooded area than any single model alone.

5. Conclusion

This study presented a multi-stage flood detection framework that integrates Sentinel-1 SAR and Sentinel-2 multispectral data within the GEE environment using machine learning and decision-level fusion. By combining complementary SAR and optical information at the data level, the proposed approach effectively exploits the strengths of different data sources. In addition, fusing the outputs of multiple classifiers using majority voting improves flood detection accuracy in semi-arid regions. The results demonstrate that decision-level fusion consistently outperforms individual classifiers, as confirmed by the employed statistical evaluation metrics. Among single classifiers, RF exhibited the strongest performance; however, the fusion strategy further improved classification reliability by reducing misclassification and resolving inconsistencies among model outputs. These findings confirm that integrating multiple machine learning classifiers can effectively mitigate the limitations of individual algorithms. The proposed framework is computationally efficient, scalable, and well-suited for rapid flood assessment, making it particularly valuable for disaster response and management applications. The use of cloud-based processing in GEE enables timely analysis over large areas without the need for extensive local computational resources. Overall, this study highlights the effectiveness of multi-stage fusion strategies for flood detection and provides a practical and transferable methodology for operational flood monitoring using freely available Earth observation data. Future research may examine decision-level fusion of deep neural networks with diverse architectures. In addition, learning-based or meta-classification approaches could be employed, where a machine or deep learning model is responsible for the fusion process to enhance robustness and generalization performance.

References

Amitrano, D., Di Martino, G., Di Simone, A., & Imperatore, P. (2024). Flood Detection with SAR: A Review of Techniques and Datasets. *Remote Sensing*, *16*(4), 656. https://doi.org/10.3390/rs16040656

Amitrano, D., Di Martino, G., Iodice, A., Riccio, D., & Ruello, G. (2018). Unsupervised Rapid Flood Mapping Using Sentinel-1 GRD SAR Images. *IEEE Transactions on Geoscience and Remote Sensing*, *56*(6), 3290–3299. https://doi.org/10.1109/TGRS.2018.2797536

Badrinarayanan, V., Kendall, A., & Cipolla, R. (2017). Segnet: A deep convolutional encoder-decoder architecture for image segmentation. IEEE transactions on pattern analysis and machine intelligence, 39(12), 2481-2495. https://doi.org/10.1109/TPAMI.2016.2644615

Brémond, P., Grelot, F., & Agenais, A. L. (2013). Review Article: Economic evaluation of flood damage to agriculture – review and analysis of existing methods. *Nat. Hazards Earth Syst. Sci.*, *13*(10), 2493–2512. https://doi.org/10.5194/nhess-13-2493-2013

Chini, M., Pelich, R., Li, Y., Hostache, R., Zhao, J., Di Mauro, C., & Matgen, P. (2021, 2021/07//). Sar-Based Flood Mapping, Where We Are and Future Challenges. 2021 IEEE International Geoscience and Remote Sensing Symposium IGARSS. https://doi.org/10.1109/igarss47720.2021.9554975

Cohen, J. (1960). A Coefficient of Agreement for Nominal Scales. Educational and Psychological Measurement, 20(1), 37–46. https://doi.org/10.1177/001316446002000104

Colacicco, R., Refice, A., Nutricato, R., Bovenga, F., Caporusso, G., D'Addabbo, A., La Salandra, M., Lovergine, F. P., Nitti, D. O., & Capolongo, D. (2024). High-Resolution Flood Monitoring Based on Advanced Statistical Modeling of Sentinel-1 Multi-Temporal Stacks. *Remote Sensing*, *16*(2), 294. https://doi.org/10.3390/rs16020294

Drusch, M., Del Bello, U., Carlier, S., Colin, O., Fernandez, V., Gascon, F., Hoersch, B., Isola, C., Laberinti, P., Martimort, P., Meygret, A., Spoto, F., Sy, O., Marchese, F., & Bargellini, P. (2012). Sentinel-2: ESA's Optical High-Resolution Mission for GMES Operational Services. Remote Sensing of Environment, 120, 25–36. https://doi.org/10.1016/j.rse.2011.11.026

Dottori, F., Szewczyk, W., Ciscar, J.-C., Zhao, F., Alfieri, L., Hirabayashi, Y., Bianchi, A., Mongelli, I., Frieler, K., Betts, R. A., & Feyen, L. (2018). Increased human and economic losses from river flooding with anthropogenic warming. *Nature Climate Change*, *8*(9), 781–786. https://doi.org/10.1038/s41558-018-0257-z

Dudy, M., Majid, S. I., Bara, A. R., Kumar, M., Kumar, R.,

& Ray, B. K. (2025). Machine Learning Driven Urban Flood Susceptibility Analysis of National Capital Territory Delhi: Integrating Remote Sensing and GIS Technique. *Journal of the Indian Society of Remote Sensing*. https://doi.org/10.1007/s12524-025-02354-1

Farhadi, H., Kiani, A., Ebadi, H., & Asgary, A. (2025). Development of an automatic time-series flood mapping framework using Sentinel-1 and 2 imagery. *Stochastic Environmental Research and Risk Assessment*, *39*(6), 2627–2655. https://doi.org/10.1007/s00477-025-02987-1

Fischer, S. (2021). Post-Disaster Spillovers: Evidence from Iranian Provinces. *Journal of Risk and Financial Management*, *14*(5), 193. https://doi.org/10.3390/jrfm14050193

Ganjirad, M., & Delavar, M. R. (2023). FLOOD RISK MAPPING USING RANDOM FOREST AND SUPPORT VECTOR MACHINE. *ISPRS Ann. Photogramm. Remote Sens. Spatial Inf. Sci.*, *X-4/W1-2022*, 201–208. https://doi.org/10.5194/isprs-annals-X-4-W1-2022-201-2023

Giustarini, L., Hostache, R., Kavetski, D., Chini, M., Corato, G., Schlaffer, S., & Matgen, P. (2016). Probabilistic Flood Mapping Using Synthetic Aperture Radar Data. *IEEE Transactions on Geoscience and Remote Sensing*, *54*(12), 6958–6969. https://doi.org/10.1109/TGRS.2016.2592951

Hajji, S., Krimissa, S., Abdelrahman, K., Boudhar, A., Elaloui, A., Ismaili, M., El Bouzekraoui, M., Chikh Essbiti, M., Kahal, A. Y., Mondal, B. K., & Namous, M. (2025). Enhancing flood prediction through remote sensing, machine learning, and Google Earth Engine [Original Research]. *Frontiers in Water, Volume 7 - 2025*. https://doi.org/10.3389/frwa.2025.1514047

Hinojosa Lee, M. C., Braet, J., & Springael, J. (2024). Performance Metrics for Multilabel Emotion Classification: Comparing Micro, Macro, and Weighted F1-Scores. Applied Sciences, 14(21), 9863. https://doi.org/10.3390/app14219863

Hitouri, S., Mohajane, M., Lahsaini, M., Ali, S. A., Setargie, T. A., Tripathi, G., D'Antonio, P., Singh, S. K., & Varasano, A. (2024). Flood Susceptibility Mapping Using SAR Data and Machine Learning Algorithms in a Small Watershed in Northwestern Morocco. *Remote Sensing*, *16*(5), 858. https://doi.org/10.3390/rs16050858

Irfan, A., Li, Y., E, X., & Sun, G. (2025). Land Use and Land Cover Classification with Deep Learning-Based Fusion of SAR and Optical Data. Remote Sensing, 17(7), 1298. https://doi.org/10.3390/rs17071298

Kazanskiy, N., Khabibullin, R., Nikonorov, A., & Khonina, S. (2025). A Comprehensive Review of Remote Sensing and Artificial Intelligence Integration: Advances, Applications, and Challenges. *Sensors*, *25*(19), 5965. https://doi.org/10.3390/s25195965

Landuyt, L., Van Wesemael, A., Schumann, G. J. P., Hostache, R., Verhoest, N. E. C., & Van Coillie, F. M. B. (2019). Flood Mapping Based on Synthetic Aperture Radar: An Assessment of Established Approaches. *IEEE Transactions on Geoscience and Remote Sensing*, *57*(2), 722–739. https://doi.org/10.1109/TGRS.2018.2860054

Lang, F., Zhu, Y., Zhao, J., Hu, X., Shi, H., Zheng, N., & Zha, J. (2024). Flood Mapping of Synthetic Aperture Radar (SAR) Imagery Based on Semi-Automatic Thresholding and Change Detection. *Remote Sensing*, *16*(15), 2763. https://doi.org/10.3390/rs16152763

Le Bris, A., Chehata, N., Ouerghemmi, W., Wendl, C., Postadjian, T., Puissant, A., Mallet, C. 2019. Decision fusion of remote-sensing data for land cover classification. In Multimodal Scene Understanding, pp. 341-382. https://doi.org/10.1016/b978-0-12-817358-9.00017-2

Liu, Y., & Huang, Y. (2020). Why Flash Floods Occur Differently across Regions? A Spatial Analysis of China. Water, 12(12), 3344. https://doi.org/10.3390/w12123344

Manavalan, R. (2016). SAR image analysis techniques for flood area mapping - literature survey. *Earth Science Informatics*, *10*(1), 1–14. https://doi.org/10.1007/s12145-016-0274-2

Manyaka, N., Shoko, C., Gxokwe, S., & Dube, T. (2026). Integrating Remote Sensing and Machine Learning for Flood Modelling: A Systematic Literature Review. *Physics and Chemistry of the Earth, Parts A/B/C*, 104315. https://doi.org/10.1016/j.pce.2026.104315

Martinis, S., Kersten, J., & Twele, A. (2015). A fully automated TerraSAR-X based flood service. *ISPRS Journal of Photogrammetry and Remote Sensing*, *104*, 203–212. https://doi.org/10.1016/j.isprsjprs.2014.07.014

Mohajane, M., Costache, R., Karimi, F., Bao Pham, Q., Essahlaoui, A., Nguyen, H., Laneve, G., & Oudija, F. (2021). Application of remote sensing and machine learning algorithms for forest fire mapping in a Mediterranean area. *Ecological Indicators*, *129*, 107869. https://doi.org/10.1016/j.ecolind.2021.107869

Morales-Barquero, L., Lyons, M. B., Phinn, S. R., & Roelfsema, C. M. (2019). Trends in Remote Sensing Accuracy Assessment Approaches in the Context of Natural Resources. Remote Sensing, 11(19), 2305. https://doi.org/10.3390/rs11192305

Peng, X., Chen, S., Miao, Z., Xu, Y., Ye, M., & Lu, P. (2025). Automatic Flood Monitoring Method with SAR and Optical Data Using Google Earth Engine. *Water*, *17*(2), 177.

https://doi.org/10.3390/w17020177

Popandopulo, G., Illarionova, S., Shadrin, D., Evteeva, K., Sotiriadi, N., & Burnaev, E. (2023). Flood Extent and Volume Estimation Using Remote Sensing Data. Remote Sensing, 15(18), 4463. https://doi.org/10.3390/rs15184463

Qin, G., Wang, S., Wang, F., Li, S., Gu, X., Chen, B., Wang, X., Wang, Z., Hu, K., & Zhu, J. (2025). Rapid flood detection in global scene based on multimodal data collaboration. *International Journal of Digital Earth*, *18*(2), 2554307. https://doi.org/10.1080/17538947.2025.2554307

Rahman, Z. U., Zhang, M., Chen, F., Ullah, S., Ahmad, M., Feroz, A., Danhassan, S. S., & Azzam, A. (2025). Flood susceptibility mapping using supervised machine learning models: insights into predictors' significance and models' performance. *Geomatics, Natural Hazards and Risk*, *16*(1), 2516728. https://doi.org/10.1080/19475705.2025.2516728

Razavi-Termeh, S. V., Sadeghi-Niaraki, A., Razavi, S., & Choi, S.-M. (2024). Enhancing flood-prone area mapping: fine-tuning the K-nearest neighbors (KNN) algorithm for spatial modelling. *International Journal of Digital Earth*, *17*(1), 2311325. https://doi.org/10.1080/17538947.2024.2311325

Razzano, F., Iandolo, M., Yogesh, G., & Ullo, S. (2023). *Integration of Sentinel-1 and Sentinel-2 data for Earth surface classification using Machine Learning algorithms implemented on Google Earth Engine*. https://doi.org/10.48550/arXiv.2308.11340

Shakya, A., Biswas, M., & Pal, M. (2021). Parametric study of convolutional neural network based remote sensing image classification. International Journal of Remote Sensing, 42(7), 2663–2685. https://doi.org/10.1080/01431161.2020.1857877

Sellami, E. M., & Rhinane, H. (2024). Google Earth Engine and Machine Learning for Flash Flood Exposure Mapping—Case Study: Tetouan, Morocco. *Geosciences*, *14*(6), 152. https://doi.org/10.3390/geosciences14060152

Shen, X., Anagnostou, E. N., Allen, G. H., Robert Brakenridge, G., & Kettner, A. J. (2019). Near-real-time non-obstructed flood inundation mapping using synthetic aperture radar. *Remote Sensing of Environment*, *221*, 302–315. https://doi.org/10.1016/j.rse.2018.11.008

Stucchi, L., Bignami, D. F., Bocchiola, D., Del Curto, D., Garzulino, A., & Rosso, R. (2021). Assessment of Climate-Driven Flood Risk and Adaptation Supporting the Conservation Management Plan of a Heritage Site. The National Art Schools of Cuba. *Climate*, *9*(2), 23. https://doi.org/10.3390/cli9020023

Tariq, M. A. U. R., Farooq, R., & van de Giesen, N. (2020). A Critical Review of Flood Risk Management and the Selection of Suitable Measures. *Applied Sciences*, *10*(23), 8752. https://doi.org/10.3390/app10238752

Tavus, B., Kocaman, S., Nefeslioglu, H. A., & Gokceoglu, C. (2020). A FUSION APPROACH FOR FLOOD MAPPING USING SENTINEL-1 AND SENTINEL-2 DATASETS. *Int. Arch. Photogramm. Remote Sens. Spatial Inf. Sci.*, *XLIII-B3-2020*, 641–648. https://doi.org/10.5194/isprs-archives-XLIII-B3-2020-641-2020

Tian, D., Wang, L., Liu, H., Cohen, S., & Shu, S. (2026). DeepSAR Flood Mapper: global flood mapping on google earth engine cloud platform using MLP deep learning model with Sentinel-1 SAR imagery and HAND topographic data. *GIScience & Remote Sensing*, *63*(1), 2612306. https://doi.org/10.1080/15481603.2025.2612306

Torres, R., Snoeij, P., Geudtner, D., Bibby, D., Davidson, M., Attema, E., Potin, P., Rommen, B., Floury, N., Brown, M., Traver, I. N., Deghaye, P., Duesmann, B., Rosich, B., Miranda, N., Bruno, C., L'Abbate, M., Croci, R., Pietropaolo, A.,…Rostan, F. (2012). GMES Sentinel-1 mission. Remote Sensing of Environment, 120, 9–24. https://doi.org/10.1016/j.rse.2011.05.028

Uddin, K., Matin, M. A., & Meyer, F. J. (2019). Operational Flood Mapping Using Multi-Temporal Sentinel-1 SAR Images: A Case Study from Bangladesh. *Remote Sensing*, *11*(13), 1581. https://doi.org/10.3390/rs11131581

Voormansik, K., Praks, J., Antropov, O., Jagomägi, J., & Zalite, K. (2014). Flood Mapping With TerraSAR-X in Forested Regions in Estonia. *IEEE Journal of Selected Topics in Applied Earth Observations and Remote Sensing*, *7*(2), 562–577. https://doi.org/10.1109/JSTARS.2013.2283340

Vongkusolkit, J., Peng, B., Wu, M., Huang, Q., & Andresen, C. G. (2023). Near Real-Time Flood Mapping with Weakly Supervised Machine Learning. Remote Sensing, 15(13), 3263. https://doi.org/10.3390/rs15133263

Wagner, W., Bauer-Marschallinger, B., Roth, F., Raiger-Stachl, T., Reimer, C., McCormick, N., Matgen, P., Chini, M., Li, Y., Martinis, S., Wieland, M., Kraft, F., Festa, D., Hassaan, M., Tupas, M. E., Zhao, J., Seewald, M., Riffler, M., Molini, L.,…Salamon, P. (2026). The fully-automatic Sentinel-1 Global Flood Monitoring service: Scientific challenges and future directions. *Remote Sensing of Environment*, *333*, 115108. https://doi.org/10.1016/j.rse.2025.115108

Willner, S. N., Levermann, A., Zhao, F., & Frieler, K. (2018). Adaptation required to preserve future high-end river flood risk at present levels. *Science Advances*. https://doi.org/10.1126/sciadv.aao1914

Yassine, L., Lakhrissi, Y., & Elhaj-Ben-Ali, S. (2024). Flood Mapping Methodologies in Google Earth

Engine Using Optical and Radar Data: A Comparative Study. *Journal of Environmental & Earth Sciences*, *7*, 363–380. https://doi.org/10.30564/jees.v7i1.7397

Yu, Q., Wang, Y., & Li, N. (2022). Extreme Flood Disasters: Comprehensive Impact and Assessment. *Water*, *14*(8), 1211. https://doi.org/10.3390/w14081211

Zaka, M. M., & Samat, A. (2024). Advances in Remote Sensing and Machine Learning Methods for Invasive Plants Study: A Comprehensive Review. *Remote Sensing*, *16*(20), 3781. https://doi.org/10.3390/rs16203781

Zainudini, M., & Sardarzaei, A. (2023). A Review of the Flood Hazard and Risk Management in The South Iran Region, Particularly Konarak, Makoran in Balochestan. British Journal of Earth Sciences Research, 11, 31–43. https://doi.org/10.37745/bjesr.2013/vol11n13143

Zhang, S., Meng, X., Liu, Q., Yang, G., & Sun, W. (2023). Feature-Decision Level Collaborative Fusion Network for Hyperspectral and LiDAR Classification. Remote Sensing, 15(17), 4148. https://doi.org/10.3390/rs15174148

Zhong, Y., Cao, Q., Zhao, J., Ma, A., Zhao, B., & Zhang, L. (2017). Optimal Decision Fusion for Urban Land-Use/Land-Cover Classification Based on Adaptive Differential Evolution Using Hyperspectral and LiDAR Data. Remote Sensing, 9(8), 868. https://doi.org/10.3390/rs9080868

Zhou, Z., Rahman Siddiquee, M. M., Tajbakhsh, N., & Liang, J. (2018, September). Unet++: A nested u-net architecture for medical image segmentation. In International workshop on deep learning in medical image analysis (pp. 3-11). Cham: Springer International Publishing. https://doi.org/10.1007/978-3-030-00889-5_1